In Situ Intercalation of Bismuth into 3D Reduced Graphene Oxide Scaffolds for High Capacity and Long Cycle-Life Energy Storage

Mengying Wang, Songlin Xie, Chengqiang Tang, Xin Fang, Meng Liao, Lie Wang, Yang Zhao, Yunzhou Wen, Lei Ye, Bingjie Wang, and Huisheng Peng**

Metal anodes, such as zinc and bismuth have been regarded as ideal materials for aqueous batteries due to high gravimetrical capacity, high abundance, low toxicity, and intrinsic safety. However, their translation into practical applications are hindered by the low mass loading (≈1 mg cm^{-2}) of active materials. Here, the multiscale integrated structural engineering of 3D scaffold and active material, i.e., bismuth is in situ intercalated in reduced graphene oxide (rGO) wall of network, are reported. Tailoring the rapid charge transport on rGO 3D network and facile access to nano- and microscale bismuth, the rGO/Bi hybrid anode shows high utilization efficiency of 91.4% at effective high load density of ≈40 mg cm^{-2}, high areal capacity of 3.51 mAh cm^{-2} at the current density of 2 mA cm^{-2} and high reversibility of >10 000 cycles. The resulting Ni-Bi full battery exhibits high areal capacity of 3.13 mAh cm^{-2} at the current density of 2 mA cm^{-2}, far outperforming the other counterpart batteries. It represents a general and efficient strategy in enhancing the battery performance by designing hierarchically networked structure.

Aqueous rechargeable batteries (ARBs) have been widely explored owing to their intrinsic safety and fast-charging performance.[1,2] An ARB with high theoretical capacity may maintain the expected high performance at low load densities of active materials,[3–6] such as <1 mg cm^{-2}. When the load densities of active materials, that are generally semiconducting or nonconducting on substrates, increase to applicable levels of >10 mg cm^{-2}, ion diffusion, electron transport, and long-term capacity retention are all largely reduced to a degree that severely challenges their practical applications.[7] It is difficult or even impossible for the produced charges to transport through relatively thick active material layers that are semiconducting or even isolating to conducting substrates.

Synthesizing active materials on 3D conducting scaffolds,[8,9] such as graphene foam[10–12] and mesoporous carbon[13–16] has been tried to reduce the severe capacity degradation. Active materials can be more loaded on the 3D conducting scaffolds,[17] and produced charges are expected to effectively transport through the 3D connected walls and channels (**Figure 1**a). However, for the thick active material layers at high load densities (Figure 1b), they would impede ion and electron accesses to the redox-active sites inside the active material, resulting in the degeneration of electrochemical performances. The thick active materials stacked on the scaffold often fall off during cycling due to the poor conductivity and large volume expansion. A protective layer such as polypyrrole sealing layer[18] was reported to be coated as the outside layer to stabilize the active materials and accommodate their volume expansions. However, the use of additional protection layer greatly reduced the capacities of ARBs. It remains challenging to achieve the desired high and stable electrochemical properties at high load densities of active materials in ARBs.

Bismuth (Bi) metal is a promising anode material in ARBs because of its high conductivity, high reversible redox reaction, wide negative window in aqueous electrolyte, and inexpensive and eco-friendly nature.[19–21] Recently, a Bi film prepared by a facile hydrothermal route exhibited high capacity of 122 mAh g^{-1} at 2 A g^{-1} and retained 60% of its capacity after 90 cycles.[22] Further the capacity was leveraged to 413 mAh g^{-1} at 39 mA g^{-1} by the introduction of rGO via a solvothermal method under nitrogen atmosphere.[23] Despite these progresses, it is still challenging for the Bi anodes to achieve high mass loading (<5 mg cm^{-2}), high areal capacity and long-term durability.

Here, we reported a one-step electro-co-reduction method to design hierarchical reduced graphene oxide/bismuth (rGO/Bi) materials with Bi intercalated between two neighboring rGO layers (Figure 1c) among the 3D framework, which increased the utilization efficiency of the 3D framework and the electron transfer efficiency. The intercalated substructure and interconnected structure offered high transports of ions for remarkable rate capacity. And Bi was bridged and stabilized by the layered rGO sheet, inhibiting it peeling off from the scaffold. As a result, recording high mass loading of 40 mg cm^{-2} and areal capacity of 3.51 mAh cm^{-2} were achieved. And a capacity retention of over 90% was maintained after 10 000 cycles.

M. Wang, S. Xie, C. Tang, Dr. X. Fang, M. Liao, L. Wang,
Y. Zhao, Y. Wen, L. Ye, Prof. B. Wang, Prof. H. Peng
Laboratory of Advanced Materials
State Key Laboratory of Molecular Engineering
of Polymers, and Department of Macromolecular Science
Fudan University
Shanghai 200438, China
E-mail: wangbingjie@fudan.edu.cn; penghs@fudan.edu.cn

The ORCID identification number(s) for the author(s) of this article can be found under https://doi.org/10.1002/smll.201905903.

DOI: 10.1002/smll.201905903

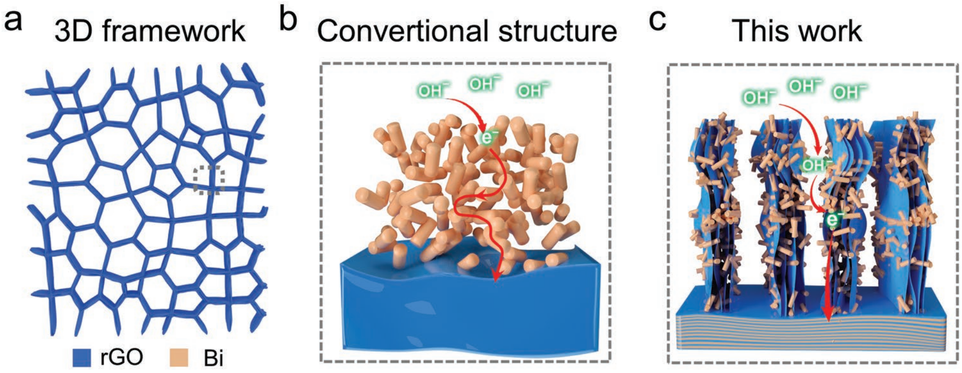

Figure 1. Schematics illustrating the electron and ion transport pathways in diverse electrodes. a) The 3D porous architecture that facilitates high mass loading and the ion diffusion. b) Illustration of the severely elongated electron and ion transport distance arising from the increased mass loading of active materials on the framework in conventional electrodes, where Bi crystals were deposited on the surface of rGO sheets. c) Rapid electron and ion transport in a thick electrode where Bi was intercalated within the multilayer rGO sheets.

The resulting Ni-Bi full battery exhibited a high areal capacity of 3.13 mAh cm^{-2} and a capacity retention of 90% after 10 000 cycles, far outperforming the other counterpart batteries. The engineering method of the material architecture may be translated into other batteries systems, and it may open up a new avenue for the development of electrochemical batteries with high mass loading.

The outperforming rate performance, reversibility and cycling stability of bismuth[20] have made it a rising star for anode materials. The closing reduction potential of Bi^{3+} (−1.2 V vs Hg/HgO electrode) with graphene oxide (GO) (−0.7 to −1.25 V vs Hg/HgO electrode) and strong electrostatic interaction between GO and Bi^{3+} (Figures S1 and S2, Supporting Information) further allowed a facile one-step electro-co-deposition to prepare rGO/Bi hybrids. GO and Bi^{3+} was simultaneously deposited on the substrate and reduced in situ at a potential of −1.2 V versus Hg/HgO electrode, forming a 3D rGO scaffold with bismuth crystals intercalated. The metal loaded on the electrode can be varied from 4 to 40 mg cm^{-2} by controlling the deposition time (Figure S3, Supporting Information).

The resulting rGO/Bi hybrid scaffold showed a macroporous structure (**Figure 2**a) with an average size of 30 µm (Figure 2b). Bismuth was deposited on the surface of rGO sheets to form submicrometer crystals (Figure 2c–h). To reveal the intrinsic growth mechanism, time lapse scanning electron microscopy (SEM) images were conducted. First, rGO sheets with Bi nucleation sites were deposited on carbon fibers in form of ribbon (Figure S4a,b, Supporting Information). Second, bismuth kept growing on nucleation sites as the rGO ribbons expanded into sheets. The rGO sheets were wrapped on single carbon fibers and joints to connect with each other to form a stable base (Figure S4c,d, Supporting Information). Third, continuous honeycomb with mono layer structure was formed (Figure S4e,f,

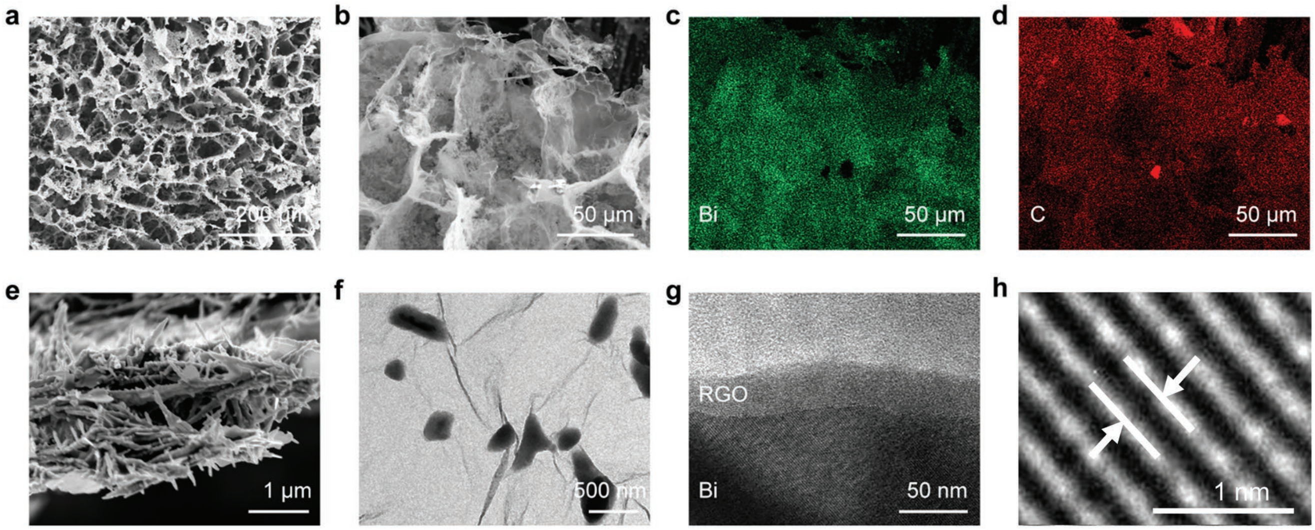

Figure 2. Structure characterizations on hierarchical rGO/Bi hybrid scaffolds. a,b) SEM images of the rGO/Bi hybrid scaffold with a load density of 6 mg cm^{-2} for the active material at low and high magnifications, respectively. c,d) Bi and C mappings of the rGO/Bi scaffold in (b). e) SEM image of a rGO/Bi scaffold where Bi crystals were deposited on the surfaces of rGO sheets. f) TEM image of Bi crystals immobilized on a rGO sheet. g) TEM image of the interface between Bi and rGO. h). Lattice structure of Bi in the rGO/Bi scaffold. The white arrows indicate the lattice space of 0.328 nm, corresponding to the (012) crystal face of Bi.

Supporting Information). The structure was found to be well maintained with the increasing mass loading (Figure S5, Supporting Information). High resolution transmission electron microscopy (TEM) image verified that the crystals on the rGO sheets corresponded to the metallic Bi, which was consistent with the X-ray diffraction (XRD) spectra (Figure S6, Supporting Information). Additionally, a special shoulder between the Bi—O and Bi—Bi scattering peak bonds in the extended X-ray absorption fine structure image revealed the possible interaction between rGO and Bi (Figure S7, Supporting Information).

To optimize the structure, we prepared rGO/Bi hybrid scaffolds with different architectures by increasing the GO concentrations from 0.01 to 0.09 mg mL^{-1}. High GO concentration introduced more rGO sheets in the scaffold, producing macropores with thicker walls (Figures S8–S11, Supporting Information). The composition of the composites can be further confirmed by thermogravimetric analysis (TGA) and Raman spectra (Figure S12, Supporting Information). In the TGA curves, the weight change at the temperature range of 250–300 °C reflected the combined result of the weight increase caused by Bi oxidation[24] and the weight decrease caused by the pyrolysis of oxygen-containing functional group on rGO.[25] In the 0.1 mg mL^{-1} group, a slight weight increase was observed, indicating the Bi oxidation dominated. With the increase of concentration of GO, the pyrolysis started to dominate and obvious weight reduction was displayed. At the temperature range of 550–620 °C, obvious weight reduction was observed attributing to the decomposition of carbon.[25] After the annealing process in TGA procedure, all the residues could be considered as Bi_2O_3 and thus the weight percentage of Bi in the composites was calculated to be 81.8%, 70.0%, 55.4%, and 55.2% at different GO concentrations of 0.01, 0.03, 0.06, and 0.09 mg mL^{-1}, respectively. The Raman spectra revealed two typical peaks of Bi located at ≈68 and 94 cm^{-1}, consistent with the characteristic E_g and A_{1g} modes of metallic Bi.[26,27] Typical peaks of rGO were also observed at ≈1340 and 1565 cm^{-1}, consistent with the D and G bands. The structural difference affected the ion transport and charge transfer at the electrode–electrolyte interface, which was confirmed by the electrochemical impedance spectroscopy (EIS). The Nyquist plots at 0 V versus Hg/HgO electrode for state of charge (SOC) 0% (**Figure 3**a) exhibited quasivertical lines in the low-frequency region (10^{-2}–10^{1} Hz), indicative of the electrical blocking behavior of porous electrodes without a charge transfer reaction.[28] The calculation method of ionic resistance (R_{ion}) from the Nyquist plots was discussed at the Supporting Information. Figure 3b clearly revealed that rGO/Bi hybrid scaffold made from 0.03 mg mL^{-1} GO had the lowest ionic resistance. Furthermore, the Nyquist plots at the charging voltage (–0.68 V vs Hg/HgO electrode) for SOC 50% (Figure 3c) showed a semicircle, where the diameter reflected the charge transfer resistance (R_{ct}). The rGO/Bi hybrid scaffold showed the lowest R_{ct} at 0.03 mg mL^{-1} (Figure 3d), which was thus used for the following discussions.

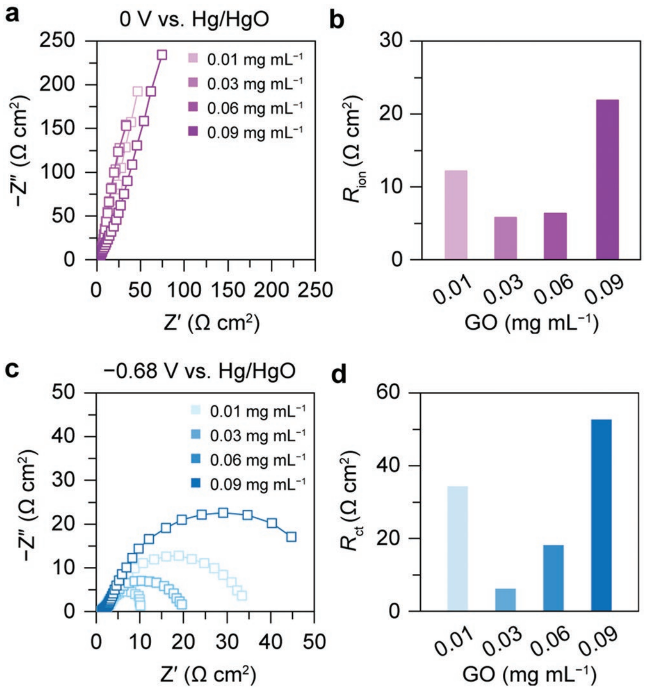

Figure 3. Kinetic properties of the rGO/Bi hybrid scaffolds with increasing rGO contents. a) Nyquist plot of rGO/Bi scaffolds with increasing rGO contents at 0 V versus Hg/HgO. b) Ionic resistance (R_{ion}) of different rGO/Bi scaffolds derived from (a). c) Nyquist plot of rGO/Bi scaffolds with increasing rGO contents at –0.68 V versus Hg/HgO. d) Charge transfer resistances (R_{ct}) of rGO/Bi scaffolds at (c).

To highlight the advantage of the rGO scaffold with intercalated Bi, we prepared another control sample (named rGO+Bi) by first electrodepositing rGO scaffold on the carbon cloth (Figure S14a–c, Supporting Information) and then electrodepositing Bi on the rGO scaffold (Figure S14d–f, Supporting Information). The rGO scaffold was covered with Bi crystals to form a stacked structure in the resulting rGO+Bi hybrid, while the Bi was intercalated into the hierarchical rGO scaffold in the rGO/Bi hybrid (**Figure 4**a). We then compared rGO+Bi and rGO/Bi hybrid electrodes in load density of active material, areal capacity, and rate performance. The rGO/Bi hybrid electrode produced much higher areal capacity with higher load density up to 40 mg cm^{-2} (Figure 4b,c). The discharge curve of the rGO/Bi electrode revealed a high IR drop of the electrode, and the electrochemical performance may be further largely enhanced with the increasing electrical conductivity of the electrode (Figure S15, Supporting Information). Figure S16 (Supporting Information) shows almost no change of the specific capacity of the rGO/Bi hybrid electrode at increasing load densities of active material, while there was a sharp decrease in the capacity of rGO+Bi hybrid electrode at high load densities.

The rGO/Bi hybrid electrode (40 mg cm^{-2}) also showed higher capacity retention at high current density (Figure 4d). At a high current density of 100 mA cm^{-2}, the rGO/Bi hybrid electrode had a reversible areal capacity of 1.5 mAh cm^{-2} and recovered to 2.5 mAh cm^{-2} when switched back to 2 mA cm^{-2}, revealing its fast reaction kinetics and high rate performance. The rapid electrochemical kinetics was further proved from the power law relationship between current density and scan rate (Figure S17, Supporting Information). And the *b* value for the rGO/Bi was 0.53, identifying the semi-infinite diffusion process.[29] In contrast, the areal capacity of the rGO+Bi hybrid electrode dropped from 0.7 mAh cm^{-2} at 2 mA cm^{-2} to 0.13 mAh cm^{-2} at 100 mA cm^{-2}. The better rate performance benefited from more

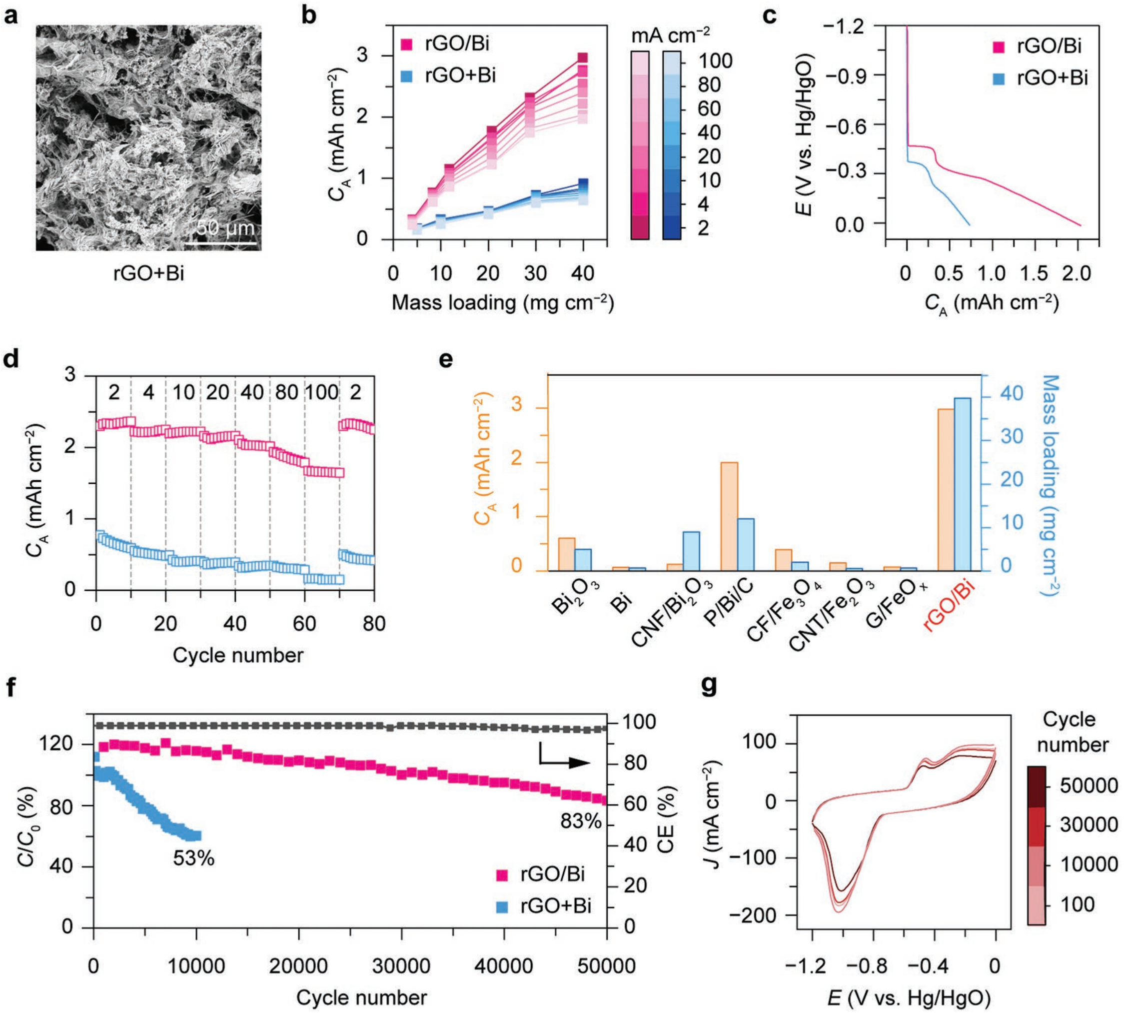

Figure 4. Comparing the rGO/Bi hybrid scaffolds with the microstructured network and rGO+Bi without the microstructured network in capacity, rate capability, and cyclic stability. a) Schematic illustration to their structure difference in the wall. b) Areal capacities of rGO/Bi and rGO+Bi scaffolds with increasing load densities at increasing current densities. c) Representative galvanostatic discharge curves of rGO/Bi and rGO+Bi hybrid electrodes at 20 mA cm^{-2} with the load density of 30 mg cm^{-2}. d) Specific capacitances of rGO/Bi and rGO+Bi hybrid electrodes with load density of 40 mg cm^{-2} at increasing discharge currents from 2 to 100 mA cm^{-2}. e) Comparison with other electrodes in areal capacity and load density (see Table S1 for details, Supporting Information). f) Cyclic stability of rGO/Bi and rGO+Bi hybrid electrodes at 100 mV s^{-1}. C represents the areal capacity after cycling, while C_0 is the initial areal capacity of the electrode. CE represents Coulombic efficiency of the rGO/Bi electrode. g) CV curves of rGO/Bi hybrid electrode after cycling.

efficient ion diffusion and electron transport derived from the 3D rGO scaffold with bismuth intercalated.

Due to its 3D scaffold and intercalated structure, the rGO/Bi hybrid electrode provided higher load density of active material for high areal capacity of 3.51 mAh cm^{-2}, which far outperforms the other electrodes for aqueous batteries (Figure 4e, details at Table S1, Supporting Information). The rGO/Bi hybrid electrode also demonstrated remarkable cyclic stability (Figure 4f). The electrode showed no obvious capacity loss even after 30 000 cycles at 100 mV s^{-1}, and retained about 83% of its original capacity even after 50 000 cycles. And the Coulombic efficiency of the electrode was stable and close to 100% during 50 000 cycling. Only a slight change of cyclic voltammetry (CV) curves was found at different cycle number (Figure 4g). In contrast, only 53% capacity was retained for the rGO+Bi hybrid electrode, and the CV curves of the rGO+Bi hybrid electrode showed a continuous and obvious capacity decay during cycling (Figure S18, Supporting Information). In addition, the cycling stability of the rGO/Bi hybrid electrode was confirmed with a continuous charging/discharging mode. The rGO/Bi hybrid electrode showed high stability with 93.4% capacity retention after 10 000 cycles (Figures S19 and S20, Supporting Information). The capacity fading may be caused by the partially irreversible and side reaction product during cycling.[20] And the intercalation of bismuth into the rGO scaffold can increased its physical confinement, and decreased the volumetric change and the dissolution of active materials during the cycling process. Inductively coupled plasma emission spectroscopy revealed the Bi concentration in the electrolyte after 50 000 cycles was 14.904 mg L^{-1} for rGO/Bi electrode, which was much lower than that after 10 000 cycles for the rGO+Bi electrode (58.794 mg L^{-1}). SEM images (Figure S21, Supporting Information) and XRD patterns (Figure S22, Supporting Information) of the rGO/Bi electrode after 1000 cycles showed well-maintained structure and composition, indicating both high reversibility of the redox reaction and stability of the structure.

Finally, we paired rGO/Bi hybrid anode with a Ni/NiO cathode to assemble Ni-Bi full battery (**Figure 5**a). The Ni/NiO electrode was prepared by electroplating Ni on a carbon cloth followed by an oxidation process[30] (Figure S23, Supporting Information). Electrochemical measurements of the Ni/NiO electrode in KOH electrolyte were conducted to match the rGO/Bi anode electrode (Figure S24, Supporting Information). The CV curve of the Ni/NiO electrode showed a prominent reduction peak at 0.22 V, representing the change between NiOOH and $Ni(OH)_2$.[31] The rGO/Bi hybrid electrode indicated a reduction peak at –0.82 V, which was caused by the change from Bi_2O_3 to Bi (Figure 5b).[19] At load density of active material of 40 mg cm^{-2} in rGO/Bi electrode, the capacities of Ni/NiO cathode and rGO/Bi hybrid anode could be well matched according to the galvanostatic charge and discharge profiles (Figure 5c). CV curves of the Ni-Bi full battery at increasing scan rates (Figure 5d) revealed well-defined redox couples, indicating rapid charge/discharge kinetics. The Ni-Bi full battery in 1 M KOH exhibited a high areal capacity of 2.86 mAh cm^{-2} at 4 mA cm^{-2} (Figure 5e). When the current density increased to 20 mA cm^{-2}, the discharge platform only decreased by 0.07 V, which revealed the good electrical conductivity of the electrodes. And a high capacity of 1.68 mAh cm^{-2} (about 60% of the initial capacity) was maintained at 100 mA cm^{-2} with a short charge/discharge time of only 60 s, manifesting its extraordinary rate performance (Figure S25, Supporting Information).

The Ni-Bi full battery delivered a volumetric energy density of 31.3 mWh cm^{-3} at the volumetric power density of 0.02 W cm^{-3}, and the volumetric energy density also exceeds the other types of aqueous batteries (Figure 5f), such as the Ni-Zn full battery (10.8 mWh cm^{-3} at 0.015 W cm^{-3}),[32] Ni-Fe full battery (5.2 mWh cm^{-3} at 0.07 W cm^{-3})[33] and Zn-MnO_2 full battery (6.3 mWh cm^{-3} at 0.46 W cm^{-3}),[34] and commercial lithium ion thin-film battery (8 mWh cm^{-3}) (Table S3, Supporting Information). Furthermore, a maximum volumetric

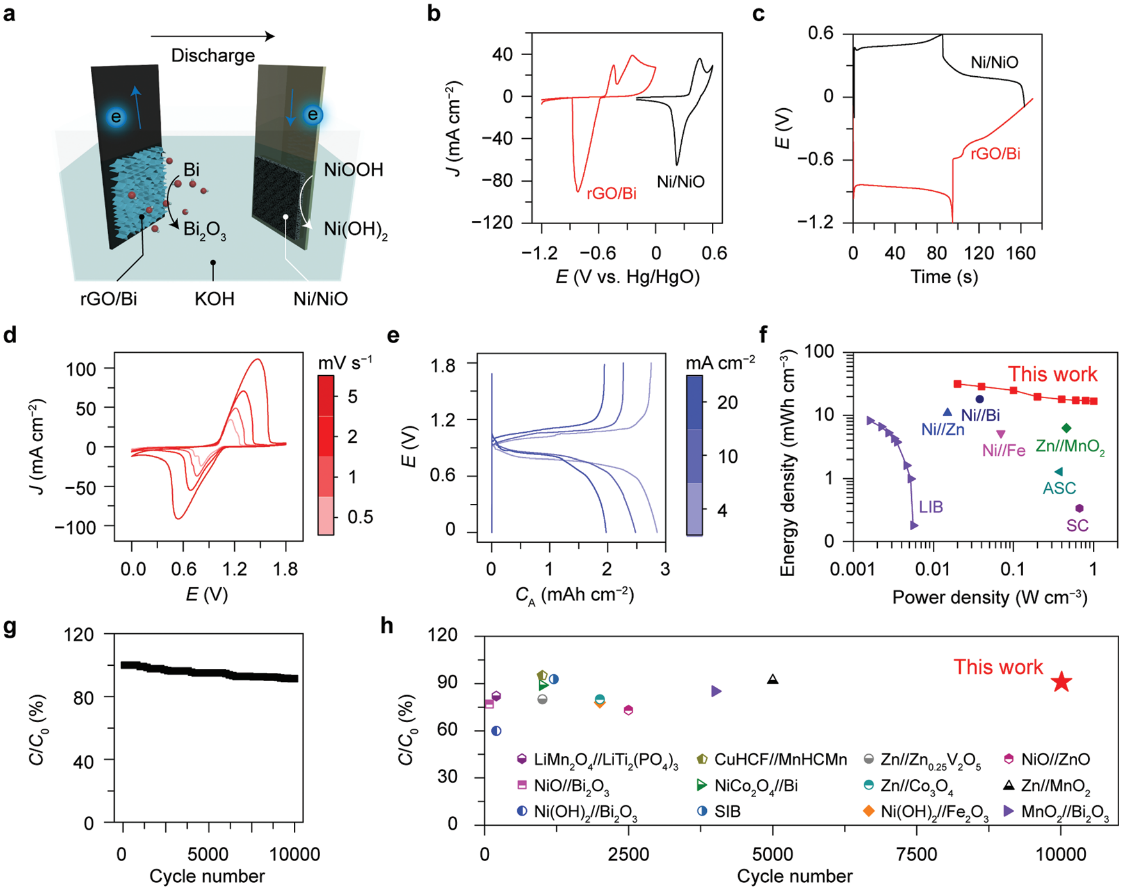

Figure 5. Electrochemical performances of the resulting Ni-Bi full battery. a) Schematic representation of a Ni-Bi full battery with rGO/Bi hybrid anode and Ni/NiO cathode. 1 M KOH was used as the electrolyte. b) CV curves of the rGO/Bi and Ni/NiO electrodes at 5 mV s^{-1}. c) Galvanostatic charge and discharge profiles of rGO/Bi hybrid and Ni/NiO electrodes at 100 mA cm^{-2}. d) CV curves of the Ni-Bi full battery at increasing scan rates. e) Galvanostatic charge and discharge profiles of the Ni-Bi full battery at increasing current densities. f) Ragone plot of the Ni-Bi full battery in this work and the other energy storage devices, such as lithium-ion battery (LIB), supercapacitor (SC), asymmetrical supercapacitor (ASC), and other metal-ion batteries (see Table S3 for details, Supporting Information). g) Cyclic stability of the Ni-Bi full battery at 10 mA cm^{-2}. *C* represents the areal capacity after cycling, while C_0 is the initial areal capacity of the battery. h) Comparison with other rechargeable full batteries in cycle performance (see Table S4 for details, Supporting Information).

power density of 1.00 W cm^{-3} was also achieved by the Ni-Bi full battery, even higher than that of commercial 3.5 V/25 mF supercapacitor (0.6 W cm^{-3}).[35] Moreover, the Ni-Bi full battery exhibited high long-term cycling stability with a capacity fading less than 9% after 10 000 cycles at 10 mA cm^{-2} (Figure 5g; and Figure S26, Supporting Information), which, to the best of our knowledge, surpasses almost all reported aqueous batteries and asymmetric supercapacitors (ASCs) (Figure 5h; and Table S4, Supporting Information).

To summarize, we designed a rGO/Bi hybrid scaffold with bismuth crystals intercalated inside the aligned rGO sheets as the anode for energy storage in aqueous electrolyte. The rGO/Bi hybrid electrode enabled high load density of active material up to 40 mg cm^{-2}, and hence high areal capacity of 3.51 mAh cm^{-2} at 2 mA cm^{-2}. This hybrid electrode also allowed rapid ion separation and charge transport, which enabled high capacity retention at high current density (1.97 mAh cm^{-2} at 100 mA cm^{-2}) and after long charge/discharge cycles (83% capacity retention after 50 000 cycles), showing good rate performance and high cyclic stability. Finally, after pairing with a Ni/NiO electrode, the resulting Ni-Bi full battery delivered a high volumetric energy density of 31.3 mWh cm^{-3} and a power density of 1.00 W cm^{-3}. Moreover, this one-step codeposition preparation method and the intercalation strategy of active materials in the 3D scaffold might apply to other metals or metal oxides and benefit both higher mass loading and areal capacity. Therefore, this work reports a new and promising strategy in the design of electrode architectures for high-performance batteries.

Experimental Section

Preparation of the rGO/Bi Hybrid Electrode: GO solution was synthesized via a modified Hummer's method.[36] The rGO/Bi hybrid scaffold was prepared on a 1 × 2 cm carbon cloth (thickness: 360 µm, WOS 1009, CeTech, 1 × 1 cm was used to load active material and 1 × 1 cm was left as electrode) by electrodeposition at 25 °C using a CHI760 electrochemical workstation. The electrodeposition was carried out in an electrolyte solution (40 mL) containing GO (0.03 mg mL^{-1}), Ethylene diamine tetraacetic acid disodium salt (EDTA·2Na) (0.1 M) and $Bi(NO_3)_3·5H_2O$ (50 × 10^{-3} M). Carbon rod and Hg/HgO electrode were used as counter and reference electrodes, respectively. A potential of –1.2 V versus Hg/HgO electrode was applied for 15 min. After electrodeposition, the sample was washed with water and dried at 80 °C in air. The mass of the rGO/Bi electrode (38.90 ± 2.00 mg cm^{-2}) was measured by an electronic balance (BT25S, 0.01 mg).

Preparation of the rGO+Bi Hybrid Electrode: As a comparison, the rGO+Bi hybrid electrode was prepared through a two-step method. First, a 3D rGO scaffold was prepared on the carbon cloth by electrodeposition in a mixture solution (40 mL) containing GO (4 mg mL^{-1}) and $LiClO_4$ (0.12 M). Carbon rod and Hg/HgO electrodes were used as counter and reference electrodes, respectively. A potential of –1.2 V was applied for 150 s. The rGO electrode was then transferred into a mixture solution containing EDTA·2Na (0.1 M), $Bi(NO_3)_3·5H_2O$ (50 × 10^{-3} M), and sodium dodecyl sulfate (50 × 10^{-3} M). Bi was deposited on the rGO scaffold by applying –0.9 V for 30 min. The sample was washed with water, dried at 80 °C in air and then measured to decide the mass with the balance.

Preparation of the Ni/NiO Electrode: Ni/NiO was prepared on a 1 × 2 cm carbon cloth (thickness: 360 µm, WOS 1009, CeTech, 1 × 1 cm was used to load active material and 1 × 1 cm was left as electrode) by electrodeposition of Ni followed by partial oxidation. The electrodeposition was conducted in an aqueous solution (40 mL) containing $NiSO_4·6H_2O$ (0.1 M), $NiCl_2·6H_2O$ (0.1 M), H_3BO_3 (0.5 M), and sodium dodecyl sulfate (35 × 10^{-3} M). Ni foam and Hg/HgO electrodes were used as counter and reference electrodes, respectively. A potential of –1.4 V was applied for 15 min. After electrodeposition, the sample was washed with water and then partially oxidized in a mixture solution containing HCl (4 M, 35 mL) and ethanol (15 mL) under sonication for 10 min. The sample was then dried in air for 30 min to obtain the Ni/NiO electrode.

Assembly of the Ni//Bi Full Battery: The Ni//Bi full battery was assembled by pairing the rGO/Bi hybrid electrode (1 × 2 cm, the thickness was 800 µm) with the Ni/NiO electrode (1 × 2 cm) in 1 M KOH aqueous solution.

Material Characterization: SEM images of the electrodes were captured on a scanning electron microscopy (Carl Zeiss Ultra 55) performed at an acceleration voltage of 5 kV. Energy dispersive spectroscopy (EDS) mappings were acquired from a scanning electron microscopy (Carl Zeiss Ultra 55) at 15 kV. TEM images were obtained from a transmission electron microscopy (FEI Tecnai G2 20 TWIN) performed at an acceleration voltage of 200 kV. Raman spectra were acquired on a confocal Raman microscope (HORIBA XploRA) using a 50× objective and 532 nm laser. The structures of materials were further characterized by X-ray photoelectron spectroscopy (XPS) (ESCALab250, Thermo VG) and XRD (D8 ADVANCE). TGA (PerkinElmer instruments Pyris) was conducted in air from room temperature to 800 °C at a heating rate of 10 °C min^{-1}. The topography and surface potential of GO sheets in the GO solution and rGO/Bi electrodepositing solution were characterized using scanning probe microscopy (Bruker Nano Inc., Multimode 8). Surface potential measurement was carried out under ambient condition using a Co-Cr coated Si probe with force constant of 2.8 N m^{-1} and a typical tip radius of ≈35 nm. The thickness was measured by the digital caliper (Shanghai constant gauge Co. LTD).

Electrochemical Measurements: CV, galvanostatic charge/discharge measurements, and electrochemical impedance spectroscopy were conducted using an electrochemical workstation (CHI 760D). The electrochemical studies of the individual electrode were carried out in a three-electrode system. The carbon cloth with active material directly served as the working electrode without any binders or conductive additives. A carbon rod was used as the counter electrode and a Hg/HgO (in 1 M KOH) as the reference electrode (+0.1 V vs SHE at 25 °C). 1 M KOH aqueous solution was used as the electrolyte. The EIS was conducted from 100 mHz to 100 kHz at a voltage amplitude of 10 mV. All electrochemical measurements of the Ni-Bi full battery were performed in 1 M KOH aqueous solution.

Supporting Information

Supporting Information is available from the Wiley Online Library or from the author.

Acknowledgements

M.W. and S.X. contributed equally to this work. This work was supported by MOST (No. 2016YFA0203302), NSFC (Nos. 21634003, 51573027, 51673043, 21604012, 21805044, and 21875042), STCSM (Nos. 16JC1400702, 17QA1400400, 18QA1400700, and 18QA1400800), SHMEC (No. 2017-01-07-00-07-E00062) and Yanchang Petroleum Group.

Conflict of Interest

The authors declare no conflict of interest.

Keywords

aqueous rechargeable batteries, hierarchical structure, high mass loading, synchronized electrodeposition

Received: October 15, 2019
Revised: November 7, 2019

[1] H. Pan, Y. Shao, P. Yan, Y. Cheng, K. S. Han, Z. Nie, C. Wang, J. Yang, X. Li, P. Bhattacharya, K. T. Mueller, J. Liu, *Nat. Energy* **2016**, *1*, 16039.
[2] H. Kim, J. Hong, K. Park, H. Kim, S. Kim, K. Kang, *Chem. Rev.* **2014**, *114*, 11788.
[3] J. Huang, Z. Wang, M. Hou, X. Dong, Y. Liu, Y. Wang, Y. Xia, *Nat. Commun.* **2018**, *9*, 2906.
[4] J. Wang, H. Tang, L. Zhang, H. Ren, R. Yu, Q. Jin, J. Qi, D. Mao, M. Yang, Y. Wang, *Nat. Energy* **2016**, *1*, 16050.
[5] H. Sun, G. Xin, T. Hu, M. Yu, D. Shao, X. Sun, J. Lian, *Nat. Commun.* **2014**, *5*, 4526.
[6] H. Wu, G. Chan, J. W. Choi, I. Ryu, Y. Yao, M. T. McDowell, S. W. Lee, A. Jackson, Y. Yang, L. Hu, *Nat. Nanotechnol.* **2012**, *7*, 310.
[7] J. Come, V. Augustyn, J. W. Kim, P. Rozier, P.-L. Taberna, P. Gogotsi, J. W. Long, B. Dunn, P. Simon, *J. Electrochem. Soc.* **2014**, *161*, A718.
[8] H. Sun, J. Zhu, D. Baumann, L. Peng, Y. Xu, I. Shakir, Y. Huang, X. Duan, *Nat. Rev. Mater.* **2019**, *4*, 45.
[9] Y. Wang, X. Fu, M. Zheng, W. H. Zhong, G. Cao, *Adv. Mater.* **2019**, *31*, 1804204.
[10] Y. Xu, Z. Lin, X. Zhong, X. Huang, N. O. Weiss, Y. Huang, X. Duan, *Nat. Commun.* **2014**, *5*, 4554.
[11] Z. Chen, W. Ren, L. Gao, B. Liu, S. Pei, H.-M. Cheng, *Nat. Mater.* **2011**, *10*, 424.
[12] B. Wang, S. Li, X. Wu, J. Liu, W. Tian, *Phys. Chem. Chem. Phys.* **2016**, *18*, 908.
[13] R. Fang, S. Zhao, P. Hou, M. Cheng, S. Wang, H. Cheng, C. Liu, F. Li, *Adv. Mater.* **2016**, *28*, 3374.
[14] T. Zuo, X. Wu, C. Yang, Y. Yin, H. Ye, N. Li, Y. Guo, *Adv. Mater.* **2017**, *29*, 1700389.
[15] Y. Zhu, X. Fan, L. Suo, C. Luo, T. Gao, C. Wang, *ACS Nano* **2016**, *10*, 1529.
[16] X. Zhang, L. Ji, O. Toprakci, Y. Liang, M. Alcoutlabi, *Polym. Rev.* **2011**, *51*, 239.
[17] M. Li, J. Meng, Q. Li, M. Huang, X. Liu, K. A. Owusu, Z. Liu, L. Mai, *Adv. Funct. Mater.* **2018**, *28*, 1802016.
[18] F. Han, D. Li, W. C. Li, C. Lei, Q. Sun, A. H. Lu, *Adv. Funct. Mater.* **2013**, *23*, 1692.
[19] Y. Zeng, Z. Lin, Y. Meng, Y. Wang, M. Yu, X. Lu, Y. Tong, *Adv. Mater.* **2016**, *28*, 9188.
[20] C. Wang, L. Wang, F. Li, F. Cheng, J. Chen, *Adv. Mater.* **2017**, *29*, 1702212.
[21] W. Zuo, W. Zhu, D. Zhao, Y. Sun, Y. Li, J. Liu, X. W. D. Lou, *Energy Environ. Sci.* **2016**, *9*, 2881.
[22] W. Zuo, P. Xu, Y. Li, J. Liu, *Nanomaterials* **2015**, *5*, 1756.
[23] T. R. Penki, G. Valurouthu, S. Shivakumara, V. A. Sethuraman, N. Munichandraiah, *New J. Chem.* **2018**, *42*, 5996.
[24] K. Nassau, A. E. Miller, E. M. Gyorgy, T. Siegrist, T. B. Laboratories, M. Hill, *J. Mater. Res.* **1989**, *4*, 1330.
[25] X. Wang, F. Xia, X. Li, X. Xu, H. Wang, N. Yang, J. Gao, *J. Nanopart. Res.* **2015**, *17*, 436.
[26] K. Trentelman, *J. Raman Spectrosc.* **2009**, *40*, 585.
[27] V. Vivier, A. Regis, G. Sagon, J.-Y. Nedelec, L. T. Yu, C. Cachet-Vivier, *Electrochim. Acta* **2001**, *46*, 907.
[28] N. Ogihara, Y. Itou, T. Sasaki, Y. Takeuchi, *J. Phys. Chem. C* **2015**, *119*, 4612.
[29] P. Hu, T. Zhu, X. Wang, X. Wei, M. Yan, J. Li, W. Luo, W. Yang, W. Zhang, L. Zhou, Z. Zhou, L. Mai, *Nano Lett.* **2018**, *18*, 1758.
[30] R. Wang, Y. Han, Z. Wang, J. Jiang, Y. Tong, X. Lu, *Adv. Funct. Mater.* **2018**, *28*, 1802157.
[31] Q. Lu, M. W. Lattanzi, Y. Chen, X. Kou, W. Li, X. Fan, K. M. Unruh, J. G. Chen, J. Q. Xiao, *Angew. Chem., Int. Ed.* **2011**, *50*, 6847.
[32] J. Liu, C. Guan, C. Zhou, Z. Fan, Q. Ke, G. Zhang, C. Liu, J. Wang, *Adv. Mater.* **2016**, *28*, 8732.
[33] C. Guan, W. Zhao, Y. Hu, Q. Ke, X. Li, H. Zhang, J. Wang, *Adv. Energy Mater.* **2016**, *6*, 1601034.
[34] Y. Zeng, X. Zhang, Y. Meng, M. Yu, J. Yi, Y. Wu, X. Lu, Y. Tong, *Adv. Mater.* **2017**, *29*, 1700274.
[35] D. Pech, M. Brunet, H. Durou, P. Huang, V. Mochalin, Y. Gogotsi, P.-L. Taberna, P. Simon, *Nat. Nanotechnol.* **2010**, *5*, 651.
[36] D. Li, M. B. Müller, S. Gilje, R. B. Kaner, G. G. Wallace, *Nat. Nanotechnol.* **2008**, *3*, 101.